Stable calcium-free myocilin olfactomedin domain variants reveal challenges in differentiating between benign and glaucoma-causing mutations

Received for publication, May 28, 2019, and in revised form, June 25, 2019 Published, Papers in Press, July 2, 2019, DOI 10.1074/jbc.RA119.009419

Shannon E. Hill[‡], Michelle S. Kwon[‡], Mackenzie D. Martin[‡], Amirthaa Suntharalingam[§], Anthony Hazel[¶], Chad A. Dickey[§†], James C. Gumbart[‡¶], and Raquel L. Lieberman[‡1]

From the Schools of [‡]Chemistry and Biochemistry and [¶]Physics, Georgia Institute of Technology, Atlanta, Georgia 30332 and [§]Department of Molecular Medicine and Byrd Alzheimer's Research Institute, University of South Florida, Tampa, Florida 33613

Edited by Paul E. Fraser

Nonsynonymous gene mutations can be beneficial, neutral, or detrimental to the stability, structure, and biological function of the encoded protein, but the effects of these mutations are often not readily predictable. For example, the β-propeller olfactomedin domain of myocilin (mOLF) exhibits a complex interrelationship among structure(s), stability, and aggregation. Numerous mutations within mOLF are linked to glaucoma; the resulting variants are less stable, aggregation-prone, and sequestered intracellularly, causing cytotoxicity. Here, we report the first stable mOLF variants carrying substitutions in the calcium-binding site that exhibit solution characteristics indistinguishable from those of glaucoma variants. Crystal structures of these stable variants at 1.8–2.0-Å resolution revealed features that we could not predict by molecular dynamics simulations, including loss of loop structure, helix unwinding, and a blade shift. Double mutants that combined a stabilizing substitution and a selected glaucoma-causing single-point mutant rescued *in vitro* folding and stability defects. In the context of full-length myocilin, secretion of stable single variants was indistinguishable from that of the WT protein, and the double mutants were secreted to varying extents. In summary, our finding that mOLF can tolerate particular substitutions that render the protein stable despite a conformational switch emphasizes the complexities in differentiating between benign and glaucoma-causing variants and provides new insight into the possible biological function of myocilin.

The effect of a nonsynonymous coding mutation on a protein can be beneficial, benign, or detrimental to downstream stability, structure, cellular trafficking, and biological function but often not in a readily predictable manner. Disease-associated proteins are commonly associated with a loss of function due to, for example, a reduction in biological activity or enhanced cellular degradation, but gain-of-toxic function, such as aggregation and cell death, is also well-established (1). At the protein level, evolutionary adaptation is for function, not overall protein stability (2, 3), as systematic studies of enzymes have revealed that charged or polar residues in sequestered active sites are optimized for catalysis (4) with compensatory mutations introduced elsewhere to balance stability (5). In cells, the molecular chaperone network detects client defects during folding and triages such proteins to enable refolding or degradation (6). Finally, the protein engineering field attempts to exploit the interplay between biophysical stability and function to improve upon or generate new biotechnologically relevant biocatalysts (7).

The ~30-kDa five-bladed β-propeller (8) olfactomedin domain of myocilin (mOLF)[2] (Fig. 1, *A* and *B*) is sensitive to mutations, many of which are causative for heritable forms of glaucoma (9). Disease-associated mOLF variants are destabilized compared with wildtype (WT) (10, 11), facilitate amyloid aggregation *in vitro* under physiological conditions (12, 13), and confer an aberrant interaction with the molecular chaperone Grp94 in cells (14). Ultimately, this leads to cytotoxicity and cell death (15) in the trabecular meshwork (TM) extracellular matrix, a key diseased ocular tissue associated broadly with glaucoma (16, 17). WT mOLF exhibits thermal stability typical of human proteins near 52 °C (18), but it too can be driven to aggregate by accessing a partially folded state via slightly elevated temperature, agitation, low pH, detergent, acid, or oxidizing or reducing agent (12, 13).

In contrast to our molecular comprehension of the role of mutations in myocilin in eliciting a glaucoma phenotype, no discrete biological function has yet been assigned to WT myocilin since its discovery 20 years ago. The diverse olfactomedin protein family is found across chordates with numerous (19, 20) subfamilies harboring different modular domains. For example, gliomedin possesses a collagen

This work was supported by National Institutes of Health Grants R01EY021205 (to R. L. L.), R01EY024232 (to C. A. D.), and R01GM123169 (to J. C. G.) and a Georgia Tech Petit undergraduate research scholarship (to M. S. K.). The authors declare that they have no conflicts of interest with the contents of this article. The content is solely the responsibility of the authors and does not necessarily represent the official views of the National Institutes of Health.

This article contains Figs. S1–S5 and Tables S1–S3.

The atomic coordinates and structure factors (codes 6OU0, 6OU1, 6OU2, and 6OU3) have been deposited in the Protein Data Bank (http://wwpdb.org/).

[†] Deceased.

[1] To whom correspondence should be addressed: School of Chemistry and Biochemistry, Georgia Institute of Technology, 901 Atlantic Dr. NW, Atlanta, GA 30332-0400. E-mail: Raquel.lieberman@chemistry.gatech.edu.

[2] The abbreviations used are: mOLF, olfactomedin domain of myocilin; MD, molecular dynamics; TM, trabecular meshwork; OLF, olfactomedin; cOLF, olfactomedin domain of collomin; r.m.s.d., root mean square deviation; PDB, Protein Data Bank; ER, endoplasmic reticulum; MBP, maltose-binding protein; BisTris, 2-[bis(2-hydroxyethyl)amino]-2-(hydroxymethyl)propane-1,3-diol; RMSF, root mean square fluctuation.

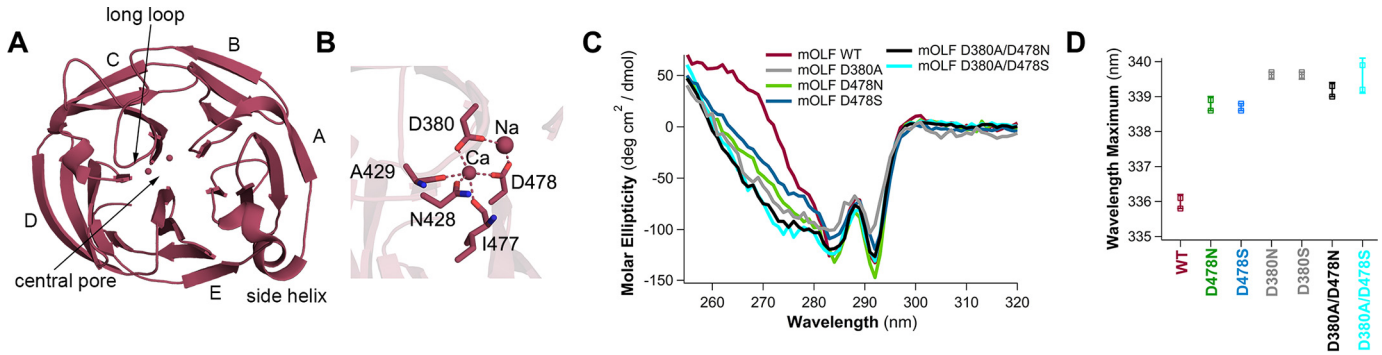

Figure 1. Stable mOLF Asp-380 and Asp-478 variants adopt a nonnative solution structure. *A*, cartoon representation and structural features of WT mOLF structure (mOLF SNP E396D, PDB code 4WXS; *dark pink*) in top-down orientation. Blades labeled A–E are centered around a solvent-filled central pore with calcium- and sodium-binding sites. *B*, zoomed-in view of the calcium and sodium environment from *A* with coordinating calcium residues highlighted. Water molecules, exclusively sodium-coordinating residues, and main chain not involved in calcium coordination were omitted for clarity. Interactions ≤2.5 Å are shown as *dashed lines*. *C*, tertiary structure signature measured by near-UV CD overlaid with disease-associated variant D380A (data from Ref. 12) shows that Asp-380 and Asp-478 variants have nonnative tertiary structure similar to D380A. *D*, wavelength position of the peak emission (λ_{max}) from excitation of intrinsic protein fluorescence reveals that Asp-380 and Asp-478 variants have a red-shifted maximum, suggesting exposed hydrophobic residues and nonnative structure. *Error bars* represent S.D. for two independent experiments. See also Figs. S1 and S2. *deg*, degrees.

domain: interaction of its trimerized OLF domain with neuronal cell adhesion molecule (21) and likely other proteins (22) aids in the molecular assembly of the nodes of Ranvier in the peripheral nervous system.

We previously observed that the *Mus musculus* olfactomedin domain of collomin (cOLF; ~25% sequence identity to mOLF; Fig. S1; 1.0-Å root mean square deviation (r.m.s.d.); Ref. 23), which falls into the gliomedin subfamily of olfactomedins and possesses a gene organization similar to the olfactomedins found in invertebrates like nematodes (19), is 20 °C more thermally stable (Table 1) and significantly more resistant to denaturation than mOLF (23). Why has nature elected to employ an aggregation-prone, disease-associated mOLF in the TM of the human eye where mutations, sustained UV exposure, and other environmental and mechanical stressors (17, 24–26) likely render myocilin susceptible to aggregation when a more stable variant like cOLF could, in theory, be resistant to these stressors and avoid disease (23)? Upon inspection of the major distinguishing structural feature in mOLF compared with cOLF, namely, the presence of a central heptacoordinate calcium ion bound in the hydrophilic central pore (Fig. 1, *A* and *B*), we considered the counterintuitive suggestion that the missing ionic interaction endows cOLF with higher stability.

Here, we probed the properties conferred by the metal-binding site on mOLF stability, structure, and cellular trafficking. Although previous work from our group indicated that the calcium site was a liability to stability (27), here we show that other mutations in the central ion-binding site are either neutral or increase thermal stability. These stable variants adopt an alternative conformation that we could not simulate *in silico*, with significant loop disorder and structural rearrangements in the first complete blade, including unwinding of the side helix. The variants are still secreted from cells when present in the context of full-length myocilin and can offset, at least to some extent, folding and secretion defects associated with selected glaucoma-causing mOLF variants. Collectively, our study offers insight into the folding and evolution of the OLF β-propeller, the relative importance of stability and structure for interactions with molecular chaperones, and the interrelationship among protein stability, native structure, and function.

Results

Calcium-ablating mOLF variants at position 380, but not at 478, are thermally compromised

In line with the nearly 40 individual mutations we introduced previously into mOLF, which had either a neutral or detrimental effect on thermal stability (8, 10, 11, 27), our knowledge of the effect of the calcium-binding site on mOLF stability and structure (Fig. 1, *A* and *B*) to date has been limited to the effect of the glaucomatous mOLF(D380A) variant, which abolished Ca^{2+} binding at the expense of ~7 °C stability (melting temperature (T_m) = 46.6 °C) (27). We had not assessed whether calcium removal depends on the particular substitution, *e.g.* D380A *versus* D380N (28), or the specific calcium ligand. However, we noticed that calcium ligands Asp-380 and Asn-428 in mOLF are largely conserved across the olfactomedin protein family, whereas Asp-478 exhibits larger variation (Fig. S2) (8). In thermostable cOLF, residues at the equivalent position of Asp-478 have side chains that cannot coordinate metals, for example alanine in human cOLF and serine in mouse cOLF (Fig. S2) (23).

Point mutants to introduce Ala, Ser, or Asn in place of Asp-380 or Asp-478 (Table 1) were generated by following established procedures (see "Experimental procedures"). In line with the results for D380A (27), changing Asp-380 to either Ser or Asn abolished calcium affinity, decreased thermal stability, and reduced soluble expression levels. Surprisingly, substitutions at Asp-478 abolished calcium binding as expected but conferred ~5–7 °C higher thermal stability than WT mOLF. Our only prior successful attempt at stabilizing mOLF was using a computational design resulting in a T_m of ~70 °C, which involved 21 simultaneous mutations (mOLF(21-variant)) with an experimentally confirmed, intact calcium site (Ref. 29 and see below).

mOLF(D478S) rescues folding and stability of glaucoma-associated variants D380A, P370L, and Y437H

The combination of the stabilizing D478S variant with selected glaucoma variants D380A, Y437H, and P370L rescues their impaired stability (Table 1). mOLF(D380A/D478S) and mOLF(D380A/D478N) are ~10 °C more stable than

Table 1
Thermal stability of OLF variants

	Motivation	T_m	ΔT_m[a]
		°C	°C
cOLF	Most thermally stable naturally occurring OLF characterized to date, no Ca^{2+} site	74.7 ± 0.5[b]	−0.4
mOLF	WT, Ca^{2+} site with ligands Asp-380, Asn-428, Asp-478	51.7 ± 0.3[c]	+7.2
mOLF(21-variant)	Computationally derived stable variant harboring Asp-380, Asn-428, Asp-478	69.8 ± 0.8[d]	+3.6
mOLF(D380A)	Glaucoma-causing variant at Ca^{2+} ligand position 380	46.6 ± 0.3[e]	−1.5
mOLF(D380N)	Glaucoma-causing variant at Ca^{2+} ligand position 380	48.0 ± 0.2	+1.0
mOLF(D380S)	Parallels D478S variant at Ca^{2+} ligand position 380	45.7 ± 0.1	−0.1
mOLF(D478A)	Residue found in human cOLF at Ca^{2+} ligand position 478	57.0 ± 0.4	+1.3
mOLF(D478N)	Parallels D380N at Ca^{2+} ligand position 478	56.4 + 0.1	+0.3
mOLF(D478S)	Residue found in mouse cOLF at Ca^{2+} ligand position 478	58.7 ± 0.4	−1.1
mOLF(D380A/D478N)	Rescue of glaucoma-causing variant D380A by stable variant D478N	55.3 ± 0.2	−1.6
mOLF(D380A/D478S)	Rescue of glaucoma-causing variant D380A by stable variant D478S	56.0 ± 0.7	−1.4
mOLF(Y437H)	Severe glaucoma-causing variant	40.3 ± 0.4[e]	+8.4
mOLF(Y437H/D478S)	Rescue of glaucoma-causing variant Y437H by stable variant D478S	46.4 ± 0.3	−0.6
mOLF(P370L)	Severe glaucoma-causing variant	NA[f]	NA
mOLF(P370L/D478S)	Rescue of glaucoma-causing variant P370L by stable variant D478S	47.0 ± 0.6	+0.9

[a] Change in T_m in the presence of 10 mM $CaCl_2$.
[b] Ref. 23.
[c] Reported value from this study. Previously reported, T_m = 53 ± 0.5 °C (27).
[d] Ref. 29.
[e] Ref. 27.
[f] NA, not available. Previously isolated as aggregated, insufficient amount of monomer for analysis (11).

mOLF(D380A), promoting mOLF(D380A/D478S or D380A/D478N) above WT mOLF stability where its aggregation propensity under physiological conditions is fully inhibited (not shown). To extend this observation, we generated additional double mutants, one harboring the severe phenotype variant P370L, which we have never been able to prepare in a folded state in *Escherichia coli* (11), and the other Y437H, a well-studied (30–32) and highly aggregation-prone (13) variant. Like mOLF(D380A/D478S), both mOLF(P370L/D478S) and mOLF(Y437H/D478S) were expressed and purified in a soluble form with reasonable yield. Thermal stabilities of these latter variants are in line with moderate glaucomatous single variants like D380A and T377M. In sum, whereas loss of calcium binding due to mutation of Asp-380 is destabilizing to mOLF, calcium ablation is not always destabilizing and in fact can be used to rescue biophysical defects of even the most deleterious glaucoma-associated variants.

Solution characterization of Asp-478 variants indicates nonnative tertiary structure

Solution biophysical characterization of Asp-478 variants reveals nonnative structure. Circular dichroism (CD) spectra of mOLF(D478S), mOLF(D478A), mOLF(D380A/D478N), and mOLF(D380A/D478S) in the regime where changes in tertiary structure can be detected (250–290 nm) reveals deviations from WT mOLF spectra, similar to glaucomatous mOLF(D380A) (Fig. 1*C*). Consistent with this result, intrinsic fluorescence reveals that both thermally stabilizing Asp-478 variants and destabilizing Asp-380 variants exhibit red-shifted fluorescence emission maxima compared with WT mOLF, indicating more exposed hydrophobic residues (Fig. 1*D*). In sum, structural changes are apparent in solution, although they cannot be distinguished from destabilized disease variants (12).

Ensemble refinement of WT mOLF structures and molecular dynamics (MD) simulations of calcium-depleted mOLF indicate modest structural fluctuations

Given the poorly predicted increase in thermal stability conferred by mutation of Asp-478 with publicly available mutant prediction servers (Table S1) and nonnative structure indicated by CD and intrinsic fluorescence, we employed MD simulations to gain insight into the structural changes that might accompany the ablation of the calcium-binding site with the introduction of Ser-478. Simulations of WT mOLF for 500 ns at T = 350 K reveal that the overall architecture remains largely unchanged, as expected for a stable protein (Figs. 2*A* and S3). The side helix (residues Ile-304–Gln-309) unravels, but no structural changes are seen in the β-sheets. These results are in line with ensemble refinement (33) of our three WT mOLF crystal structures (8), which reveals fluctuations in three loops (residues Thr-261–Lys-266, Thr-290–Asp-294, and Tyr-442–Ala-445; Fig. 2*B* and Table S2). Next, we compared these results with the scenario in which the calcium ion was removed from the WT mOLF structure. Unexpectedly, MD simulations indicate a rigidification of numerous loops. In the environs of the calcium site, we observed conformational changes to Asn-428, Asp-380, and Ala-429, presumably as an attempt to accommodate repulsion from the negatively charged, calcium-coordinating side chains remaining upon removing the ion; the motion of Asn-428 is most dramatic (Figs. 2, *C* and *E*, and S3*B*). Finally, we conducted MD simulations on the D478S variant by mutating the WT mOLF structure after removal of calcium (Figs. 2, *D* and *E*, and S3*B*). Excluding the increased motion observed for the loop composed of residues Thr-290–Asp-294, as seen in the ensemble refinement of WT mOLF, the simulations again reveal a rigidification of loops, such as for the long loop (residues Ile-360–Gly-375; Fig. 1*A*) on the top face of the propeller. Overall, ensemble refinement of WT mOLF crystal structures and MD simulations of WT mOLF and relevant variants indicate changes in flexibility of the loops but do not suggest gross structural rearrangements, at least on the sub-μs time scale.

Comparisons of mOLF(D478S), mOLF(D478N), mOLF(D380A/D478S), and mOLF(21-variant) with WT mOLF structures reveal localized blade shift, helix unfolding, and loop disorder

To reconcile these apparent contradictions at the molecular level, we solved crystal structures of mOLF(D478S), mOLF(D478N), and mOLF(D380A/D478S), each at 1.8–2.0-Å resolution (Table 2). The Asp-478 variants overlay

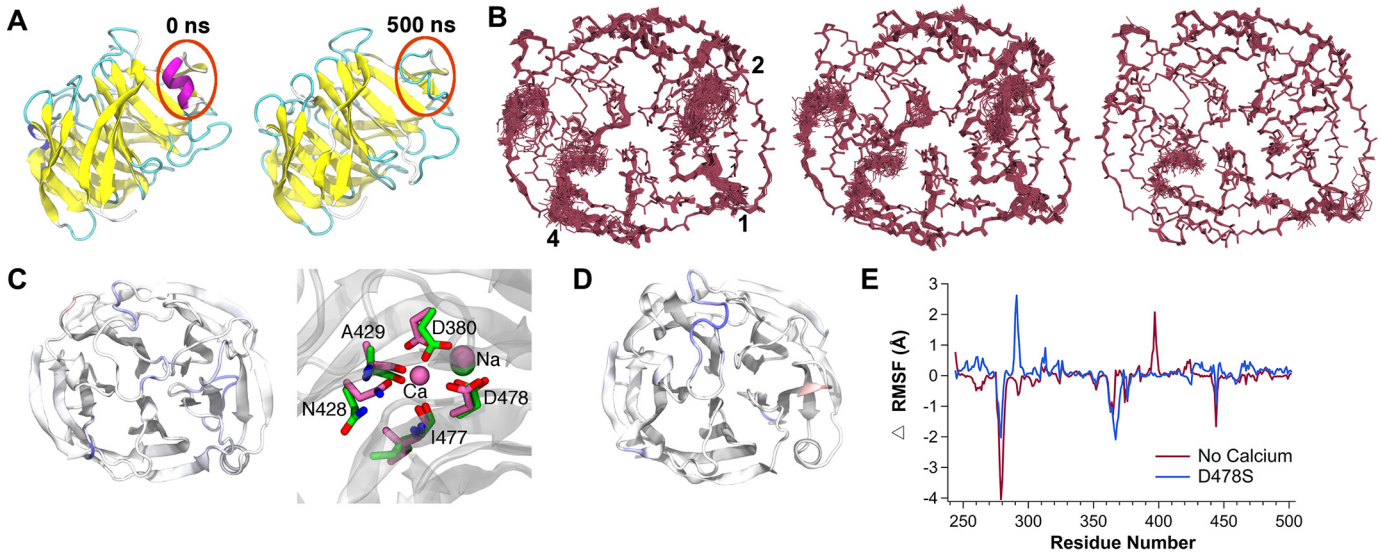

Figure 2. MD simulations and ensemble refinement of WT mOLF suggest only limited loop fluctuations. *A*, simulated unfolding of WT mOLF shows the side helix (Fig. 1*A* and region 3 in Fig. 3) is the first to unfold at elevated temperature. *B*, WT mOLF crystal structures (*left* to *right*, PDB codes 4WXS, 4WXQ, and 4WXU) after ensemble refinement, displayed as main-chain lines for each state, are relatively compact with small fluctuations in three loops. Loops are defined in Figs. 3 and 4 as loop/helix region 1 (residues Thr-261–Lys-266), loop region 2 (residues Thr-290–Asp-294), and loop region 4 (residues Tyr-442–Ala-445). *C*, MD simulations after removal of calcium from WT mOLF suggest that overall loops become more rigid (*left*). In the calcium environment (*right*), side chains of coordinating residues Asn-428 and Asp-380 shift positions (*pink*, WT mOLF; *green*, after calcium removal and simulation). *D*, MD simulations of WT mOLF in which Asp-478 is replaced with serine reveal increased mobility for loop region 2 (residues Thr-290–Asp-294) but no overall changes in secondary structure. For *C* (*left*) and *D*, residues are colored according to positive (*red*) and negative (*blue*) difference in per-residue root mean square fluctuations (ΔRMSF) values. *E*, ΔRMSF during MD simulations between RMSF of WT mOLF and RMSF of WT mOLF without calcium as in *C* (*dark pink*) and D478S variant as in *D* (*blue*). See also Fig. S3 and Table S2.

Table 2

Data collection and refinement statistics

Statistics for the highest-resolution shell are shown in parentheses. CC1/2, Pearson correlation coefficient between random half data sets; CC*, modification of CC1/2; CC(work) and CC(free), correlation coefficient of the observed to the model-based intensities.

	D478N	D478S	D380A/D478S	21-variant
Data collection statistics				
PDB code	6OU2	6OU3	6OU0	6OU1
Wavelength	1.0	1.0	1.0	1.0
Resolution range	40.26–1.96 (2.03–1.96)	35.55–1.80 (1.86–1.80)	35.38–1.80 (1.86–1.80)	36.71–1.88 (1.95–1.88)
Space group	P 21 21 21	P 21 21 21	P 21 21 21	P 1 21 1
Unit cell (Å; °)	45.0, 57.3, 90.4; 90, 90, 90,	45.4, 57.2, 90.5; 90, 90, 90	45.2, 56.9, 90.3; 90, 90, 90	43.4, 66.9, 80.1; 90, 95.2, 90
Total reflections	116,956 (6,115)	255,594 (21,668)	267,804 (26,279)	140,324 (9,605)
Unique reflections	17,169 (1,633)	22,530 (2,139)	22,208 (2,164)	34,931 (2,963)
Multiplicity	6.8 (3.8)	11.3 (10.1)	12.1 (12.1)	4.0 (3.4)
Completeness (%)	99.6 (96.7)	99.6 (97.1)	99.70 (98.54)	90.99 (69.48)
Mean $I/\sigma(I)$	16.7 (4.8)	15.0 (2.9)	18.67 (4.27)	11.98 (2.49)
Wilson B-factor	18.54	15.79	17.57	21.47
R_{merge}	0.1324 (0.4908)	0.1266 (0.6122)	0.09304 (0.4396)	0.1018 (0.5508)
R_{meas}	0.1431 (0.5632)	0.1326 (0.6439)	0.09724 (0.4587)	0.1172 (0.6494)
R_{pim}	0.0534 (0.2686)	0.0389 (0.1957)	0.02784 (0.1295)	0.05675 (0.3348)
CC1/2	0.996 (0.77)	0.998 (0.925)	0.999 (0.966)	0.992 (0.541)
CC*	0.999 (0.933)	1 (0.98)	1 (0.991)	0.998 (0.838)
Refinement statistics				
Reflections used in refinement	17,202 (1,633)	22,526 (2,138)	22,207 (2,164)	34,331 (2,598)
Reflections used for R_{free}	1,721 (163)	1,999 (190)	2,000 (195)	1,886 (141)
R_{work}	0.1661 (0.1888)	0.1496 (0.1925)	0.1608 (0.1863)	0.1676 (0.2228)
R_{free}	0.1976 (0.2198)	0.1733 (0.2482)	0.1888 (0.2374)	0.1950 (0.2531)
CC (work)	0.956 (0.899)	0.965 (0.942)	0.963 (0.948)	0.958 (0.854)
CC (free)	0.947 (0.862)	0.966 (0.856)	0.960 (0.831)	0.938 (0.855)
Number of non-hydrogen atoms	2,170	2,184	2,159	4,437
Macromolecules	1,998	1,969	1,955	4,132
Ligands	7	13	6	16
Solvent	165	202	198	289
Protein residues	249	246	244	515
r.m.s. (bonds)	0.004	0.008	0.005	0.005
r.m.s. (angles)	1.05	1.16	1.04	1.03
Ramachandran favored (%)	96.30	97.48	97.03	96.46
Ramachandran allowed (%)	2.88	2.52	2.97	3.34
Ramachandran outliers (%)	0.82	0.00	0.00	0.20
Rotamer outliers (%)	0.92	0.93	0.47	0.67
Clashscore	5.32	4.86	5.43	2.70
Average B-factor	26.26	24.11	25.48	29.37
Macromolecules	25.91	23.23	24.80	28.99
Ligands	20.76	39.81	33.45	31.19
Solvent	30.68	31.62	31.85	34.61

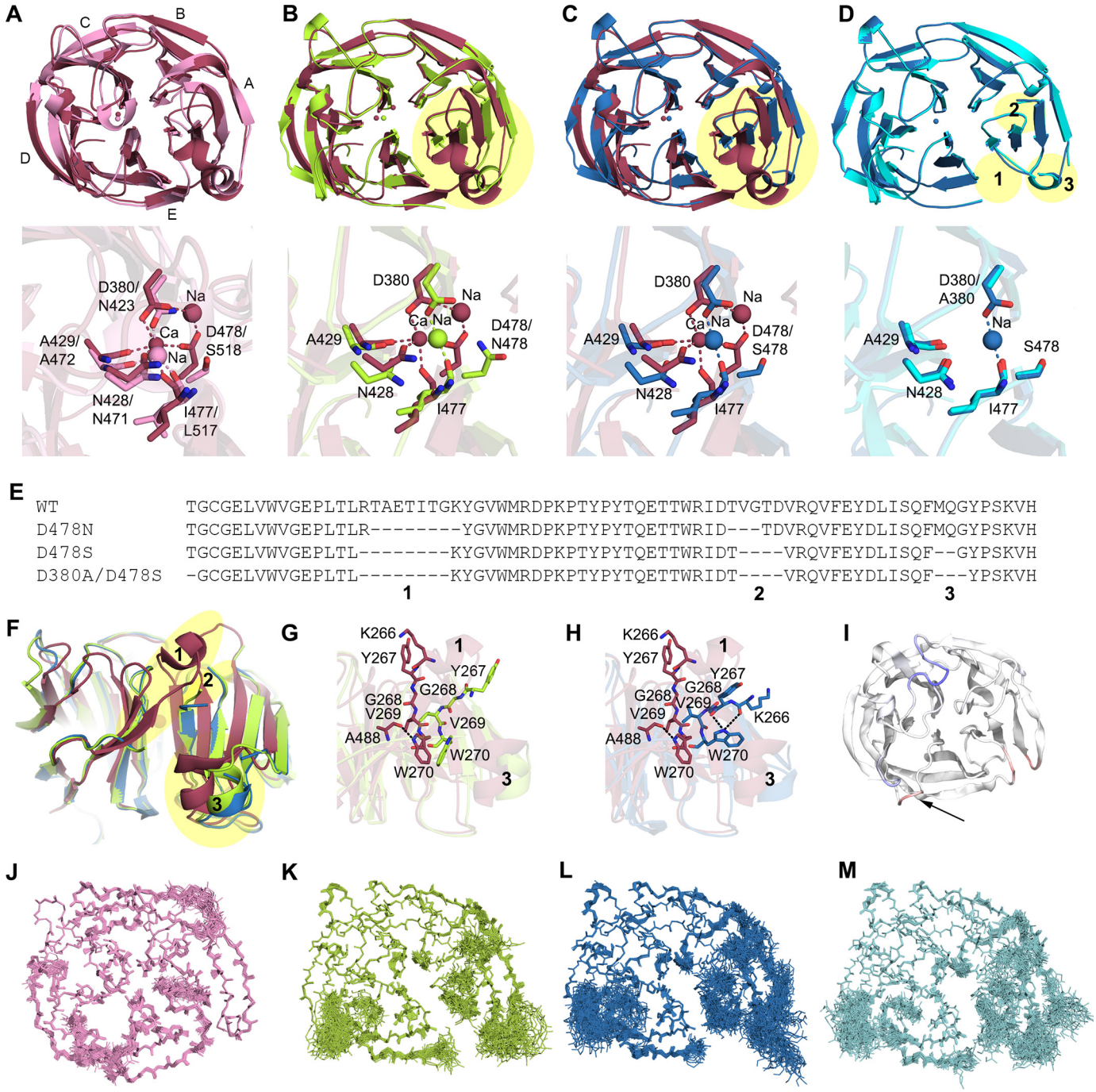

Figure 3. Structures of stable mOLF variants D478N, D478S, and D380A/D478S show altered ion-binding sites, loop, and helix structures compared with WT mOLF and cOLF. *A–C*, *top panel*, cartoon representation of WT mOLF top face (mOLF SNP E396D, PDB code 4WXS; *dark pink*) with blades labeled A–E compared with cOLF (*light pink*) (*A*), D478N (*green*) (*B*), and D478S (*dark blue*) (*C*). *D*, *top*, cartoon representation of D478S compared with D380A/D478S (*light blue*). *A–D*, *bottom panel*, zoomed-in view of the calcium and sodium environment with coordinating residues highlighted as in Fig. 1*B*. *E*, sequence alignment of structural residues visible at the N terminus and within blade A. Regions labeled *1–3* (loop/helix region 1, loop region 2, and side helix region 3) are highlighted in *D*. *F*, side view of helix comparing WT mOLF, D478N, and D478S. Regions labeled *1–3* show significant changes in loop and/or helix structure. *G* and *H*, zoomed-in view of the interacting residues with visible electron density following loop/helix region 1. For D478N (*G*), Trp-270 orientation is nonnative but within the hydrophobic pocket, whereas for D478S (*H*), Trp-270 is in a completely new position. *I*, removal of side helix region 3 in MD simulations of WT mOLF reveals movement near the side helix and helix/loop region 1 but also in more spatially distant regions, such as loop Asn-469–Tyr-473, which is also shifted in the Asp-478 variant structures (*arrow*). *J–M*, ensemble refinement, displayed as main-chain lines for each state, of cOLF (*J*), mOLF(D478N) (*K*), mOLF(D478S) (*L*), and mOLF(D380A/D478S) (*M*). See also Fig. S3 and Table S2.

with WT mOLF (r.m.s.d. of ~1.3 Å) but adopt an alternative conformation. In the mOLF(D478N) and mOLF(D478S) central pore, a metal ion is present, but not in the same position as the WT mOLF Ca^{2+} or Na^+ or cOLF Na^+ (Fig. 3, *A–C*). Instead, for mOLF(D478N) and mOLF(D478S), an ion assigned as Na^+ coordinates the side chain of Asp-380 as well as the carbonyl oxygen of Ile-477 and six water molecules, whereas for mOLF(D380A/D478S), ions are not coordinated (Fig. 3*D*). For all Asp-478 variant structures, blades B–E are superimposable, but for blade A, there is a ~2-Å

shift of all four strands away from the central pore. Alignment of the isolated four strands of blade A of Asp-478 variants and WT structures reveals that the blade is superimposable (r.m.s.d. of 0.16 Å (not shown)). Along with the blade A shift is an increase in disorder for connecting loops (labeled loop/helix region 1, Thr-261–Lys-266, and loop region 2, Thr-290–Asp-294; Fig. 3, *D* and *E*) and unraveling of the side helix (labeled side helix region 3, Ile-304–Gln-309; Figs. 1*A* and 3, *D–F*). We note that the extent to which we could fit models to electron density in these mobile regions (Figs. 3*E* and S4, *A–C*) was inversely correlated with rank order of thermostability when comparing mOLF(D478N) or mOLF(D478S) with mOLF(D380A/D478S) (Table 1). A major shift of Trp-270 from being nestled in a hydrophobic pocket near Leu-257, Phe-307, and Phe-487 to an exposed conformation along with changes to Tyr-267 and Trp-489 in the Asp-478 variants (Fig. 3, *G* and *H*) likely contributes to the observed nonnative CD spectra (Fig. 1*C*). MD simulations recapitulate this loss of electron density; if side helix region 3 (Ile-304–Gln-309) is removed from WT mOLF, increased mobility is observed for the loops of blades A and E (Fig. 3*I*) along with the shift in blade A as seen for Asp-478 variants (Fig. S3*C*). Still, the structures do not provide a clear reason for higher thermostability of the Asp-478 variants compared with WT. The overall contact order is similar (not shown), and although significant increased flexibility is detected upon ensemble refinement of mOLF(D478N), mOLF(D478S), and mOLF(D380A/D478S) compared with the otherwise well-ordered WT mOLF and cOLF structures (Figs. 2*B* and 3, *J–M*, and Table S2), chemical intuition would dictate that the combination of the loss of ordered loops and helical secondary structure would correspond to a less, not more, thermostable protein.

For further comparison, we next solved the 1.9-Å-resolution structure of our most stable mOLF variant to date (29), which harbors 21 computationally predicted mutations (Table 2 and Figs. 4*A* and S4*D*). The two monomers present in the asymmetric unit are more similar to WT than the Asp-478 variants with an overall r.m.s.d. of just 0.7–0.8 Å, but they each also exhibit unexpected alternative conformations (Fig. 4*B*). The monomer assigned as chain A is fully modeled, and blades overlay well with WT mOLF, but ensemble analysis reveals flexibility in the same three loops seen as disordered or missing among the Asp-478 variant structures (Fig. 4*C*). The second monomer, chain B, lacks density for residues 261–264, and ensemble refinement supports thermal motions in the loops of blades D, E, and A (Fig. 4*D* and Table S2). We surmise that substitution of L492G and possibly N493H weaken the hydrophobic interactions in blade E (Fig. 4, *E* and *F*), which propagate to neighboring blades D and A.

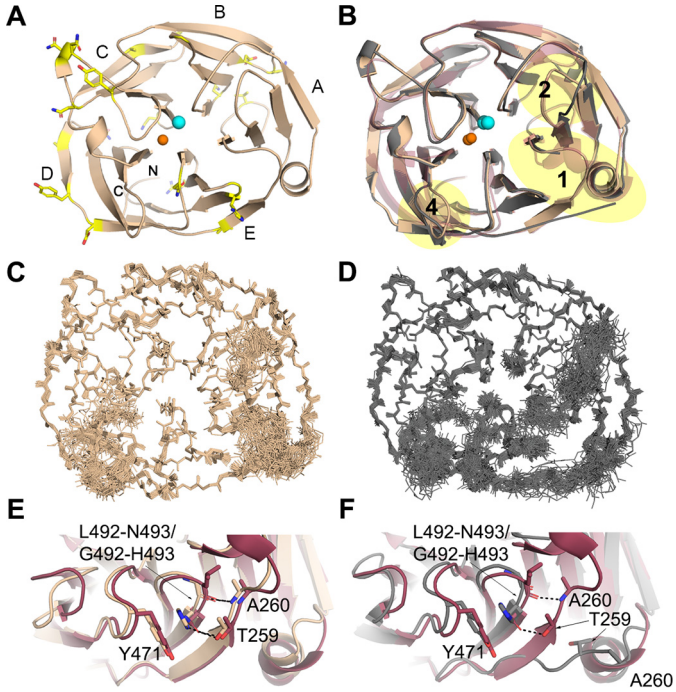

Figure 4. Crystal structure of thermally stable mOLF(21-variant) reveals distinct conformations for each monomer in the asymmetric unit. *A*, cartoon representation of monomer A (*beige*; blades labeled A–E) with location of amino acids (*yellow sticks*) that differ from WT mOLF. *Orange sphere*, Ca^{2+}; *cyan sphere*, Na^{+}. *B*, superposition of monomer A, monomer B (*gray*), and WT mOLF (mOLF SNP E396D, PDB code 4WXS; *dark pink* as in Fig. 3; *partially transparent*). Monomer A is nearly indistinguishable from WT mOLF, whereas monomer B exhibits three loop changes, *circled* in *pale yellow* and *numbered 1* and *2* as in Fig. 3 and *4* as in Fig. 2 involving Tyr-442 previously shown to have alternative conformations for WT mOLF (8). *C* and *D*, ensemble refinement, displayed as main-chain lines for each state, of monomer A (*C*) reveals a similar degree of flexibility as compared with WT mOLF (Fig. 2*B*) with some degree of flexibility for loop/helix region 1 (residues Thr-261–Lys-266), loop region 2 (residues Thr-290–Asp-294), side helix region 3 (residues Ile-304–Gln-309), and loop region 4 (residues Tyr-442–Ala-445). Ensemble refinement of monomer B (*D*) shows a longer stretch of flexibility between the N terminus and loop/helix region 1 (residues Thr-261–Lys-266) as revealed by a compromised molecular clasp in the initial refinement and additional flexibility for loop Asn-469–Tyr-473, which is shifted in the Asp-478 variant structures (Fig. 3, *B* and *C*). *E* and *F*, enlarged region 1 from *B*. *E*, monomer A and WT mOLF share interactions for the molecular clasp in blade E. Monomer A has an additional π–π stacking interaction between His-493 and Tyr-471 that is not present in WT mOLF. *F*, in monomer B, the molecular clasp is compromised, indicated by loss of H-bonding, an alternative conformation for the first β-strand of blade E, and loss of electron density for loop/helix region 1 (residues Thr-261–Lys-266) leading to blade A.

Alternative conformation adopted by stable Asp-478 variants bolsters evolutionary relationship of OLF to six-bladed propellers

Previously, a phylogenetic relationship between the OLF propeller and six-bladed propellers was suggested based on close structural similarity for blades A–D with a six-bladed Kelch domain (34). Evolutionary classification of protein domains based on structure (35) identifies a six-bladed propeller (DUF4221; PDB code 3S9J), a domain of unknown function from the bacterium *Bacteroides vulgatus* ATCC 8482, at a branchpoint with OLFs (Fig. S5*A*). Although the overall r.m.s.d. for the two domains remains ~3 Å, the ~2-Å shift of blade A observed in mOLF Asp-478 variants results in a visually better superposition to the six-bladed propeller (PDB ID 3S9J) than with WT mOLF (Fig. S5, *B* and *C*). Perhaps by adopting a more ancestral-like fold (36), namely closer to a six-bladed propeller, the stable mOLF Asp-478 variants exhibit increased thermostability even while ablating an ionic interaction and weakening certain intermolecular interactions as these features were added later as the propeller acquired new function.

Cellular secretion profiles of stable single-point Asp-478 variants are indistinguishable from WT myocilin and when combined with glaucoma-causing variants rescue secretion to varying degrees

Myocilin is a component of the TM extracellular matrix and is thus secreted from TM cells. Disease-associated mutations

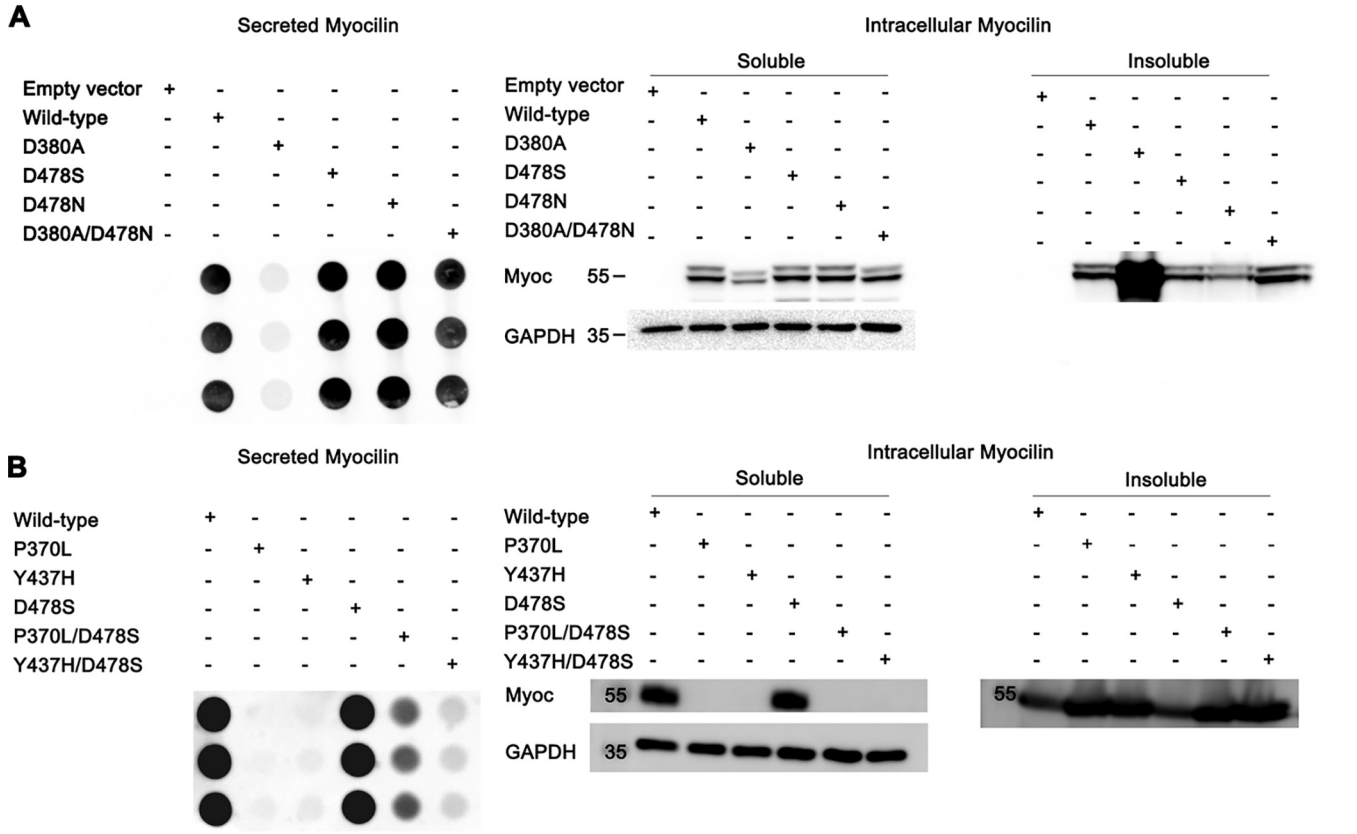

Figure 5. Cellular secretion assays of full-length myocilin variants reveal that stabilizing mutations can, to varying extents, rescue secretion of glaucoma-associated variants. Dot blot analyses (*left panels*) of secreted myocilin (*Myoc*) from spent media from transfected HEK293T cells is compared with Western blot analyses of detergent-soluble and -insoluble lysates (*right panels*). *A*, secretion and intracellular aggregate profiles of stable variants (D478N and D478S); a moderately stable, disease-associated variant (D380A); and a combination variant (D380A/D478N), which is rescued to a large extent. *B*, secretion and intracellular aggregate profiles of a stable variant (D478S); severely destabilized, glaucoma-associated variants (P370L and Y437H); and combination variants (P370L/D478S and Y437H/D478S), which are rescued to lesser extents than D380A/D478N in *A*. Labeled molecular mass markers are in kDa. Ponceau staining (dot blot; data not shown) and glyceraldehyde-3-phosphate dehydrogenase (*GAPDH*) (Western blotting) were used as loading controls.

are instead sequestered intracellularly (15, 30, 37, 38), specifically within the ER (39), not the cytosol (40). Misfolded myocilin is recognized by the molecular chaperone Grp94 as not competent for secretion, but instead of undergoing efficient degradation, aggregated mutant myocilin accumulates, leading to ER stress, TM cell death (8, 15, 41), and a cascade that results in early onset ocular hypertension, the causal risk factor for glaucoma.

We compared the cellular secretion profiles of WT and characterized mOLF calcium variants in the context of full-length myocilin using a HEK293 transiently transfected cell culture model, probing both extracellular and intracellular levels of myocilin (Fig. 5). The stable variants, D478S and D478N, which adopt a non-WT structure (Fig. 3), are secreted as for WT myocilin, with only low levels of soluble and insoluble intracellular myocilin detected. Thus, the non-native structure exhibited by the calcium-free variants is not recognized by chaperone machinery, allowing these proteins to proceed through the secretory pathway.

Next we examined the secretion profile of myocilin double mutants that rescued folding and thermal stability of glaucoma-causing variants in the context of purified mOLF (see Table 1). Myocilin single-point variants D380A, P370L, and Y437H were sequestered intracellularly with aggregates that are insoluble in detergent as reported previously (30). Of the three double mutants tested, only secretion of D380A/D478N (Fig. 5*A*), which has WT-like mOLF stability, was rescued to near WT levels. By contrast, P370L/D478S and Y437H/D478S, which have lower overall stability, are secreted to a lesser degree (Fig. 5*B*).

Discussion

The OLF β-propellers comprise a structurally distinct five-bladed family; data in this study along with previous observations support the hypothesis that OLF evolved from more common six-bladed propellers. Olfactomedins are unusual in that they are only found in multicellular organisms, and although they are associated with numerous human diseases, explicit biological functions have not been assigned for most subfamily members (42). For myocilin, the high sensitivity of mOLF to destabilization and misfolding due to mutation is well-documented (11) and is causative for ocular hypertension and familial glaucoma (43); however, its function has remained elusive since its discovery 20 years ago. In our original mOLF structures, we trapped slightly different conformations of well-ordered loops in different crystal forms, but neither these structures nor computational analyses presented in this study predicted that mutation of Asp-478 would lead to a more stable, secreted variant, much less one adopting an alternative conformation with a high degree of new localized flexibility.

Partially folded but stable mOLF domain variants

Our current study demonstrates the complex relationship among mutations, structure, stability, and aggregation and elevates the need to more closely probe the relationship between location of mutation and glaucoma pathogenesis. The effects of a mutation on mOLF stability and folding are more complex than we appreciated until now. Indeed, our ability to use chemical intuition in predicting the consequences of other mutations in mOLF is relatively limited. Our early attempts to correlate stability effects of mutation and location in the mOLF structure did not define clusters very well (8), and using this analysis we predicted that Asp-478 variants would behave as D380A, a well-studied destabilized, aggregation-prone glaucoma variant. The disease association of any given myocilin mutation for glaucoma is not definitive because without a confirmed family history, variations in myocilin are not a common cause of glaucoma (44). Successful clinical implementation of therapeutic strategies under development, namely eliminating mutant myocilin by CRISPR (45) or promoting myocilin degradation through manipulation of ER chaperone machinery (14, 46, 47), will rely heavily on accurate assessments of likelihood of pathogenicity of an identified myocilin mutation.

Our study also raises the intriguing possibility that the helix unwinding observed for Asp-478 variants is accessible in WT mOLF upon a functionally relevant stimulus. Regulated helix unwinding, also termed helix cracking, is known in the context of signal modulation in other proteins (48–50), including propagation via coiled coils (51), which are found in myocilin. In addition, large kinetic barriers can prevent facile interconversion between two stable conformations of a protein that require a trigger, like for hemagglutinin (52). In this study, we discovered that the mOLF calcium-binding site is not always a liability in terms of thermal stability and that the presence of central calcium-mediated ionic interactions imparts the helix-wound WT mOLF structure but at the expense of thermal stability. This observation is in line with the general observation that proteins of mesophilic origin are thought to be marginally stable because there is no selection advantage for higher stability, only function (53), suitable levels of plasticity (54), and regulation (2).

Perhaps extracellular myocilin is responsive to calcium levels, such as fluxes associated with TM contractility (17, 55). Namely, myocilin may be spring-loaded, detecting mechanical stimuli in the form of calcium flux and converting this signal to a structural readout (56). Such mechanotransduction would be tightly controlled as it might affect multiple aspects of TM function and could involve a variety of extracellular proteins (57). Although in the laboratory calcium is only fully removed from purified WT mOLF under denaturing conditions (27) and Asp-380 and Asp-478 would experience charge repulsion when in close proximity, calcium depletion could result in an alternative metal ion center within the pore, for example, by shuffling the ligands binding Na^+ and Ca^{2+}. Our MD simulations indicated a shift for calcium ligands when Ca^{2+} is removed, and we can envision Asp-380 switching from binding Ca^{2+} to a buried Lys-423. This would further require movement of Tyr-371, which forms a cation–π interaction with Lys-423 in our WT mOLF structure and is ~2-Å shifted in the D478S structure. Propagation of these motions to N-terminal surface loops as seen in mOLF(D478S) and MD simulations might increase the surface accessibility of essential residues to interact with functionally relevant binding partners. In support of this proposal, the N-terminal ~50 amino acids of mOLF share less similarity with cOLF than the remaining ~200 residues, and connecting loops are consistently 1–3 residues longer than those of cOLF (Figs. 3*A* and S1).

The suggestion that a D478S-like conformation is functionally relevant may explain why these variants are competent for secretion even though in solution their *in vitro* CD profiles are indistinguishable from disease variants. The full complement of molecular chaperones inspecting myocilin during folding in TM cells is not established, but our study demonstrates that achieving native structure of mOLF with well-buried hydrophobic residues is not a strict requirement for myocilin secretion. Rather, the varying extents of secretion for the double mutants D478N/D380A, D478S/P370L, and D478S/Y437H suggest that a thermal stability threshold exists for recognition by a molecular chaperone, perhaps as a correlate of corresponding aggregation propensity. Future detailed investigations of myocilin trafficking, for both WT and D478S-like conformations, are warranted to establish whether kinetics (58, 59) or binding partners also influence secretion.

In sum, our study reveals a conformation of mOLF that is distinct from the destabilized conformation leading to amyloidogenic aggregation or a molten globule competent for folding (60). The thermostable, calcium-free mOLF single-point variants are secreted from cells like WT myocilin even though *in vitro* solution characterization resembles those of destabilized glaucoma variants. Partially unfolded protein variants are typically less stable than the well-folded native state, but examples exist where alternative conformations are functional. The alternative conformation we captured in our study by ablating calcium binding in mOLF is likely accessible even without mutation, upon a calcium flux or mechanical stimulus or upon binding a ligand or partner protein. These new structural insights bring us closer to identifying the biological function of this cryptic β-propeller.

Experimental procedures

Molecular biology

The parent WT mOLF plasmid was generated as reported previously with a maltose-binding fusion protein and factor Xa cleavage site (10). Variants of mOLF were prepared by site-directed mutagenesis according to the manufacturer's protocol (QuikChange Lightening kit). Forward and reverse primers (Table S3) specific for each mOLF variant were designed using Agilent Technologies QuikChange Primer Design and purchased from MWG Operon. Fidelity of plasmid sequences was confirmed by DNA sequencing (MWG Operon).

Protein expression

Plasmids were transformed into Rosetta-Gami 2 competent cells onto agar plates containing 60 μg/ml ampicillin and 34 μg/ml chloramphenicol selective LB broth. Starter cultures were prepared by adding one bacterial colony of mOLF variant to 250 ml of LB medium containing selective ampicillin/chloramphenicol antibiotics followed by incubation at 37 °C with

shaking overnight (225–250 rpm). For large-scale cultures, 25 ml of the starter culture was used to inoculate each 1-liter solution of Superior broth in 2-liter baffled flasks, and the solutions were allowed to grow at 37 °C in a shaking incubator (225–250 rpm) until the cells reached an optical density (OD) of ~1.5–1.7 measured at 600 nm. At this point, the temperature was reduced to 18 °C, flasks were equilibrated for 1.5 h at 18 °C, and protein expression was induced with 500 μM isopropyl β-D-thiogalactopyranoside. The cells continued to incubate overnight at 18 °C for 16–18 h. The next day, the cells were harvested by centrifugation (2,380 × *g*) with 10-min spins, flash frozen with liquid nitrogen, and stored at −80 °C.

Purification of mOLF variants

MBP-mOLF variant cells (3 g) were resuspended in 10 ml of amylose wash buffer (10 mM Na_2HPO_4, 10 mM KH_2PO_4, 200 mM NaCl, 1 mM EDTA) with 1× cOmplete protease inhibitor mixture (Roche Applied Science) and lysed by passage through a French press twice. Cell debris was removed by centrifugation at 161,716 × *g* at 4 °C for 45 min. The soluble fraction was loaded onto an amylose-affinity column (New England Biolabs) equilibrated with amylose wash buffer, and MBP-mOLF fusion protein was eluted with amylose elution buffer (10 mM Na_2HPO_4, 10 mM KH_2PO_4, 200 mM NaCl, 1 mM EDTA, 10 mM maltose). Final fractionation using a Superdex 75 (GE Healthcare) size-exclusion column equilibrated with gel filtration buffer (10 mM Na_2HPO_4, 10 mM KH_2PO_4, 200 mM NaCl) isolated monomeric MBP-mOLF variants. MBP-mOLF variants were then cleaved with factor Xa (New England Biolabs) in a 50:1 protein-to-factor Xa reaction solution for 18 h at room temperature. Amylose-affinity chromatography was then used to separate cleaved mOLF variants. The mOLF variants were further polished by a final Superdex 75 followed by purity assessment with 12% resolving SDS-PAGE.

Thermal stability measurements

Each mOLF variant was tested for thermal stability by differential scanning fluorimetry as described previously (10). Briefly, purified mOLFs were buffer-exchanged into 10 mM HEPES, pH 7.5, 200 mM NaCl by concentrating and diluting three times using an Amicon 10,000 molecular-weight-cutoff filtration device. Reaction mixtures (30 μl) containing 1× SYPRO Orange and a final protein concentration of 3 μM were prepared in triplicate at room temperature with or without 10 mM $CaCl_2$. Samples were placed in a 96-well optical plate (Applied Biosystems) and sealed with optical film. Fluorescence measurements were obtained on an Applied Biosciences Step-One Plus real-time PCR instrument. Melts were conducted from 25 to 95 °C with a 1 °C/min increase. Data were analyzed using Origin software (OriginLab Corp.). The T_m was calculated at the midpoint of unfolding using a Boltzmann sigmoid equation. Reported values are an average of two independent experiments.

CD

Near-UV CD measurements were acquired on a Jasco J-815 spectropolarimeter equipped with a Jasco PTC-4245/15 temperature control system. mOLF samples at a concentration range between 1.0 and 3.5 mg/ml were measured in gel filtration buffer at 4 °C. Scans were acquired from 250 to 320 nm at a rate of 50 nm/min and a data pitch of 1 nm using a 0.1-cm cuvette. Each measurement was an average of 20 scans. Data were blank-subtracted and converted to mean residue ellipticity $\Theta = \text{Mres} \times \Theta\text{obs}/10 \times d \times c$ where Mres = 112.9 is the mean residue mass calculated from the protein sequence, Θobs is the observed ellipticity (°) at wavelength λ, *d* is the pathlength (cm), and *c* is the protein concentration (g/ml). The reported spectra are an average of two independent measurements.

Intrinsic fluorescence measurements

Intrinsic fluorescence of purified mOLF at 1 μM protein concentration in gel filtration was measured on a Shimadzu RF-5301PC spectrofluorophotometer at an excitation wavelength of 284 nm and an emission wavelength range of 300–500 nm with 5-nm slit widths on excitation and emission monochromators. Spectra were collected nine times in 0.2-nm data intervals and averaged. Each variant was measured in triplicate. Reported values are an average of two independent experiments.

MD simulations

The WT mOLF structure (PDB code 4WXQ) (8) was used for MD simulations. The visualization and analysis program VMD (61) was used to solvate the system with ~14,500 TIP3P (62) water molecules in an 80 × 75 × 85-$Å^3$ box. The system was then neutralized with 0.15 M KCl, resulting in a final system size of ~48,000 atoms. Residue deletions and mutations were performed on the WT mOLF structure as described in the text.

MD simulations were carried out using NAMD 2.12 (63) and AMBER 16 (64) running on both CPUs and GPUs. The CHARMM36 force field was used for proteins (65). The temperature was maintained using Langevin dynamics; the pressure was kept at 1 atm using the Langevin piston method (66). The equations of motion were integrated using the RESPA multiple time-step algorithm with a time step of 2 fs for all bonded interactions, 2 fs for short-range nonbonded interactions, and 4 fs for long-range electrostatic interactions. Long-range electrostatic interactions were calculated using the particle-mesh Ewald method (67). Bonds involving hydrogen atoms were constrained to their equilibrium length. All mOLF systems were first allowed to equilibrate for 1 ns at 310 K with backbone atoms restrained before production simulations at 350 K. WT mOLF was simulated for 500 ns; all other mOLF variants were simulated for 100 ns.

Crystallization of mOLF(D478S), mOLF(D478N), mOLF(D380A/D478S), and mOLF(21-variant)

Crystallization of mOLF(D478S), mOLF(D478N), mOLF(D380A/D478S), and mOLF(21-variant), all concentrated to 15 mg/ml except mOLF(21-variant), which was concentrated to 9 mg/ml in 10 mM HEPES, pH 7.5, was optimized from the condition used to crystallize purified selenomethionine (SeMet)-substituted mOLF(E396D) (8). Crystals were grown by the hanging-drop method with a 1:1 drop ratio of well solution to protein. mOLF(D478N) crystals were grown at room temperature in 20% PEG 3350, 0.2 M BisTris, pH 6.0, 0.3 M magnesium formate, whereas mOLF(21-variant) crystals, also at room temperature,

were grown in 20% PEG 3350, 0.2 M BisTris, pH 6.0, 0.1 M magnesium formate. mOLF(D478N) and mOLF(21-variant) were cryoprotected in 15% PEG 3350, 0.1 M BisTris, pH 6.0, 0.1 M magnesium formate, 25% glycerol. mOLF(D478S) crystals were grown at 4 °C in 20% PEG 3350, 0.2 M BisTris, pH 6.0, 0.4 M magnesium formate, whereas mOLF(D380A/D478S) crystals, also at 4 °C, were grown in 15% PEG 3350, 0.2 M BisTris, pH 6.0, 0.2 M magnesium formate. mOLF(D478S) and mOLF(D380A/D478S) were cryoprotected in their respective mother liquor components supplemented with 25% glycerol.

Diffraction data were collected at the Southeast Regional Collaborative Access Team (SER-CAT) 22-ID beamline and processed using HKL-2000 (68). The mOLF(D380A/D478S) and mOLF (21-variant) structures were solved by molecular replacement using Phaser (69) with the mOLF(E396D) crystal structure (PDB code 4WXS) as the search model followed by Phenix AutoBuild for mOLF(D380A/D478S) (70). The mOLF(D478S) and mOLF(D478N) structures were solved by molecular replacement using the refined mOLF(D380A/D478S) structure as the search model in Phaser. The models were iteratively built and refined using Coot (71) and phenix.refine (72).

Ensemble refinement

Phenix.ensemble_refinement was performed on WT/E396D mOLF (PDB codes 4WXQ, 4WXS, and 4WXU), cOLF (4XAV), mOLF(D478N), mOLF(D478S), mOLF(D380A/D478S), and mOLF(21-variant) using the default Phenix parameters plus translation-libration-screw-rotation (TLS) optimization. Prior to ensemble refinement of 4WXU, 4WXS, and 4WXQ, phenix.ReadySet was performed after removal of alternative conformations in PDB code 4WXU and renaming of chains in PDB code 4WXQ.

Cellular secretion assay

HEK293T cells were grown and maintained in Dulbecco's modified Eagle's medium supplemented with 10% fetal bovine serum (Sigma), 1% sodium pyruvate (Corning), and 1% GlutaMAX (Invitrogen) at 37 °C under 5% CO_2. For Fig. 5*A*, 6.5×10^5 cells/well and for Fig. 5*B*, 5.0×10^5 cells/well were plated 24 h prior to DNA transfection. Plasmid transfections were carried out in serum-free Opti-MEM (Invitrogen) medium via lipofection. A 1 μg:2.5 μl ratio of plasmid:Lipofectamine 2000 was used. Cells were transfected 48 h prior to harvest with pRc/CMV expression vector encoding tagless myocilin (Fig. 5*A*) or with pcDNA 4 expression vector encoding C-terminal FLAG-tagged myocilin (Fig. 5*B*). For Fig. 5*B*, all reagents remained the same except medium was supplemented with 10% fetal bovine serum (HyClone) including 1% penicillin/streptomycin (Gibco).

Media from cells were collected and spun at 10,000–16,000 × *g* for 10 min. 200 μl of media supernatant (Fig. 5*A*) or 7 μl of media supernatant diluted into 100 μl of nuclease-free water (Fig. 5*B*) was added into each well of a GE Healthcare dot blot apparatus and suctioned onto a nitrocellulose membrane. The membrane was then washed with PBS (filtered) twice and placed in Ponceau S to confirm the presence of protein followed by blocking with 5–7% milk for 1 h.

For intracellular fractionation to detect insoluble myocilin, cells were lysed either in 100 μl of Triton X-100 lysis buffer (100 mM Tris-HCl, pH 7.4, 3 mM EGTA, 5 mM $MgCl_2$, 0.5% Triton X-100) containing protease inhibitor mixture (Calbiochem) and 1× phosphatase inhibitor II and III mixtures (Sigma) (Fig. 5*A*) or in 100 μl of Mammalian Protein Extraction Reagent (M-PER) (Pierce) lysis buffer with 1× cOmplete protease inhibitor mixture and 1× phosphatase inhibitor II and III mixtures (Fig. 5*B*). Lysed cells were centrifuged at 10,000–16,000 × *g* for 10 min. Equal amounts of soluble supernatant from cell lysates were prepared with 2× Laemmli sample buffer (Bio-Rad) containing 2-mercaptoethanol and denatured by boiling for 5 min at 100 °C or 10 min at 95 °C. For the insoluble faction presented in Fig. 5*A*, the pellet was washed with ice-cold PBS and then resuspended in 2× Laemmli sample buffer with 9 M urea followed by sonication and denaturation by boiling. For Fig. 5*B*, the pellet was resuspended in equal volumes of Triton X-100 lysis buffer and 2× Laemmli sample buffer with 2-mercaptoethanol and 8 M urea. Samples were then sonicated using a tip sonicator for 3 min with 10-s on/off pulses at 50% amplitude and then boiled in a 95 °C water bath for 10 min. Prepared soluble and insoluble samples were then loaded onto a 10% Tris-glycine SDS-polyacrylamide gel. Gels were transferred onto polyvinylidene difluoride membranes (Millipore) and blocked for 1 h at room temperature with 5–7% milk prior to Western blotting.

A myocilin polyclonal antibody gifted from Dr. Dan Stamer (Duke University) was used to image blots presented in Fig. 5*A* (1:3,000 dilution and 1:3,000 dilution of secondary antibody in 7% milk), and the myocilin mAb (R&D Systems, catalog number MAB3446, RRID:AB_2148649) was used for Fig. 5*B* (1:1,000 dilution and 1:5,000 dilution of secondary antibody in 1% milk). Glyceraldehyde-3-phosphate dehydrogenase antibody was purchased from Meridian Life Science (catalog number H86903M, RRID:AB_936702; Fig. 5*A*) and Cell Signaling Technology (catalog number 51332, RRID:AB_2799390; Fig. 5*B*). Horseradish peroxidase–linked secondary antibodies were purchased from Southern Biotechnologies (catalog number 1010-05, RRID:AB_2728714; Fig. 5*A*) and Thermo Fisher Scientific (catalog number 62-6520, RRID:AB_2533947; Fig. 5*B*).

Author contributions—S. E. H., M. S. K., M. D. M., and J. C. G. conceptualization; S. E. H., M. S. K., M. D. M., A. S., A. H., C. A. D., and R. L. L. data curation; S. E. H., C. A. D., J. C. G., and R. L. L. formal analysis; S. E. H., M. S. K., M. D. M., C. A. D., J. C. G., and R. L. L. supervision; S. E. H., M. D. M., C. A. D., J. C. G., and R. L. L. funding acquisition; S. E. H. and M. S. K. validation; S. E. H., M. S. K., M. D. M., A. S., A. H., C. A. D., J. C. G., and R. L. L. investigation; S. E. H., M. S. K., M. D. M., A. H., J. C. G., and R. L. L. methodology; S. E. H., M. S. K., and R. L. L. writing-original draft; S. E. H., M. S. K., and R. L. L. writing-review and editing; J. C. G. and R. L. L. project administration.

Acknowledgments—We thank the Petit Institute Core Facility for access to instrumentation. Southeast Regional Collaborative Access Team (SER-CAT) is supported by its member institutions and National Institutes of Health Equipment Grants S10_RR25528 and S10_RR028976. Use of the Advanced Photon Source was supported by the United States Department of Energy, Office of Science, Office of Basic Energy Sciences, under Contract W-31-109-Eng-38.

References

1. Valastyan, J. S., and Lindquist, S. (2014) Mechanisms of protein-folding diseases at a glance. *Dis. Model. Mech.* **7,** 9–14 CrossRef Medline
2. DePristo, M. A., Weinreich, D. M., and Hartl, D. L. (2005) Missense meanderings in sequence space: a biophysical view of protein evolution. *Nat. Rev. Genet.* **6,** 678–687 CrossRef Medline
3. Schreiber, G., Buckle, A. M., and Fersht, A. R. (1994) Stability and function: two constraints in the evolution of barstar and other proteins. *Structure* **2,** 945–951 CrossRef Medline
4. Shoichet, B. K., Baase, W. A., Kuroki, R., and Matthews, B. W. (1995) A relationship between protein stability and protein function. *Proc. Natl. Acad. Sci. U.S.A.* **92,** 452–456 CrossRef Medline
5. Wang, X., Minasov, G., and Shoichet, B. K. (2002) Evolution of an antibiotic resistance enzyme constrained by stability and activity trade-offs. *J. Mol. Biol.* **320,** 85–95 CrossRef Medline
6. Balchin, D., Hayer-Hartl, M., and Hartl, F. U. (2016) *In vivo* aspects of protein folding and quality control. *Science* **353,** aac4354 CrossRef Medline
7. Bloom, J. D., Labthavikul, S. T., Otey, C. R., and Arnold, F. H. (2006) Protein stability promotes evolvability. *Proc. Natl. Acad. Sci. U.S.A.* **103,** 5869–5874 CrossRef Medline
8. Donegan, R. K., Hill, S. E., Freeman, D. M., Nguyen, E., Orwig, S. D., Turnage, K. C., and Lieberman, R. L. (2015) Structural basis for misfolding in glaucoma-associated myocilin. *Hum. Mol. Genet.* **24,** 2111–2124 CrossRef Medline
9. Wiggs, J. L., and Pasquale, L. R. (2017) Genetics of glaucoma. *Hum. Mol. Genet.* **26,** R21–R27 CrossRef Medline
10. Burns, J. N., Orwig, S. D., Harris, J. L., Watkins, J. D., Vollrath, D., and Lieberman, R. L. (2010) Rescue of glaucoma-causing mutant myocilin thermal stability by chemical chaperones. *ACS Chem. Biol.* **5,** 477–487 CrossRef Medline
11. Burns, J. N., Turnage, K. C., Walker, C. A., and Lieberman, R. L. (2011) The stability of myocilin olfactomedin domain variants provides new insight into glaucoma as a protein misfolding disorder. *Biochemistry* **50,** 5824–5833 CrossRef Medline
12. Hill, S. E., Donegan, R. K., and Lieberman, R. L. (2014) The glaucoma-associated olfactomedin domain of myocilin forms polymorphic fibrils that are constrained by partial unfolding and peptide sequence. *J. Mol. Biol.* **426,** 921–935 CrossRef Medline
13. Orwig, S. D., Perry, C. W., Kim, L. Y., Turnage, K. C., Zhang, R., Vollrath, D., Schmidt-Krey, I., and Lieberman, R. L. (2012) Amyloid fibril formation by the glaucoma-associated olfactomedin domain of myocilin. *J. Mol. Biol.* **421,** 242–255 CrossRef Medline
14. Suntharalingam, A., Abisambra, J. F., O'Leary, J. C., 3rd, Koren, J., 3rd, Zhang, B., Joe, M. K., Blair, L. J., Hill, S. E., Jinwal, U. K., Cockman, M., Duerfeldt, A. S., Tomarev, S., Blagg, B. S., Lieberman, R. L., and Dickey, C. A. (2012) Glucose-regulated protein 94 triage of mutant myocilin through endoplasmic reticulum-associated degradation subverts a more efficient autophagic clearance mechanism. *J. Biol. Chem.* **287,** 40661–40669 CrossRef Medline
15. Liu, Y., and Vollrath, D. (2004) Reversal of mutant myocilin non-secretion and cell killing: implications for glaucoma. *Hum. Mol. Genet.* **13,** 1193–1204 CrossRef Medline
16. Clark, A. F. (2012) The cell and molecular biology of glaucoma: biomechanical factors in glaucoma. *Invest. Ophthalmol. Vis. Sci.* **53,** 2473–2475 CrossRef Medline
17. Liton, P. B., and Gonzalez, P. (2008) Stress response of the trabecular meshwork. *J. Glaucoma* **17,** 378–385 CrossRef Medline
18. Orwig, S. D., and Lieberman, R. L. (2011) Biophysical characterization of the olfactomedin domain of myocilin, an extracellular matrix protein implicated in inherited forms of glaucoma. *PLoS One* **6,** e16347 CrossRef Medline
19. Zeng, L. C., Han, Z. G., and Ma, W. J. (2005) Elucidation of subfamily segregation and intramolecular coevolution of the olfactomedin-like proteins by comprehensive phylogenetic analysis and gene expression pattern assessment. *FEBS Lett.* **579,** 5443–5453 CrossRef Medline
20. Li, Q., Liu, A., Gu, X., and Su, Z. (2019) Olfactomedin domain-containing proteins: Evolution, functional divergence, expression patterns and damaging SNPs. *Mol. Genet. Genomics*, 1–11 CrossRef Medline
21. Eshed, Y., Feinberg, K., Carey, D. J., and Peles, E. (2007) Secreted gliomedin is a perinodal matrix component of peripheral nerves. *J. Cell Biol.* **177,** 551–562 CrossRef Medline
22. Rasband, M. N., and Peles, E. (2015) The nodes of Ranvier: molecular assembly and maintenance. *Cold Spring Harb. Perspect. Biol.* **8,** a020495 CrossRef Medline
23. Hill, S. E., Donegan, R. K., Nguyen, E., Desai, T. M., and Lieberman, R. L. (2015) Molecular details of olfactomedin domains provide pathway to structure-function studies. *PLoS One* **10,** e0130888 CrossRef Medline
24. Acott, T. S., Kelley, M. J., Keller, K. E., Vranka, J. A., Abu-Hassan, D. W., Li, X., Aga, M., and Bradley, J. M. (2014) Intraocular pressure homeostasis: maintaining balance in a high-pressure environment. *J. Ocul. Pharmacol. Ther.* **30,** 94–101 CrossRef Medline
25. Keller, K. E., Kelley, M. J., and Acott, T. S. (2007) Extracellular matrix gene alternative splicing by trabecular meshwork cells in response to mechanical stretching. *Invest. Ophthalmol. Vis. Sci.* **48,** 1164–1172 CrossRef Medline
26. Sacca, S. C., Bolognesi, C., Battistella, A., Bagnis, A., and Izzotti, A. (2009) Gene-environment interactions in ocular diseases. *Mutat. Res.* **667,** 98–117 CrossRef Medline
27. Donegan, R. K., Hill, S. E., Turnage, K. C., Orwig, S. D., and Lieberman, R. L. (2012) The glaucoma-associated olfactomedin domain of myocilin is a novel calcium binding protein. *J. Biol. Chem.* **287,** 43370–43377 CrossRef Medline
28. Challa, P., Herndon, L. W., Hauser, M. A., Broomer, B. W., Pericak-Vance, M. A., Ababio-Danso, B., and Allingham, R. R. (2002) Prevalence of myocilin mutations in adults with primary open-angle glaucoma in Ghana, West Africa. *J. Glaucoma* **11,** 416–420 CrossRef Medline
29. Goldenzweig, A., Goldsmith, M., Hill, S. E., Gertman, O., Laurino, P., Ashani, Y., Dym, O., Unger, T., Albeck, S., Prilusky, J., Lieberman, R. L., Aharoni, A., Silman, I., Sussman, J. L., Tawfik, D. S., *et al.* (2016) Automated structure- and sequence-based design of proteins for high bacterial expression and stability. *Mol. Cell* **63,** 337–346 CrossRef Medline
30. Vollrath, D., and Liu, Y. (2006) Temperature sensitive secretion of mutant myocilins. *Exp. Eye Res.* **82,** 1030–1036 CrossRef Medline
31. McDowell, C. M., Luan, T., Zhang, Z., Putliwala, T., Wordinger, R. J., Millar, J. C., John, S. W., Pang, I. H., and Clark, A. F. (2012) Mutant human myocilin induces strain specific differences in ocular hypertension and optic nerve damage in mice. *Exp. Eye Res.* **100,** 65–72 CrossRef Medline
32. Zode, G. S., Kuehn, M. H., Nishimura, D. Y., Searby, C. C., Mohan, K., Grozdanic, S. D., Bugge, K., Anderson, M. G., Clark, A. F., Stone, E. M., and Sheffield, V. C. (2011) Reduction of ER stress via a chemical chaperone prevents disease phenotypes in a mouse model of primary open angle glaucoma. *J. Clin. Investig.* **121,** 3542–3553 CrossRef Medline
33. Levin, E. J., Kondrashov, D. A., Wesenberg, G. E., and Phillips, G. N., Jr. (2007) Ensemble refinement of protein crystal structures: validation and application. *Structure* **15,** 1040–1052 CrossRef Medline
34. Han, H., and Kursula, P. (2015) The olfactomedin domain from gliomedin is a β-propeller with unique structural properties. *J. Biol. Chem.* **290,** 3612–3621 CrossRef Medline
35. Cheng, H., Schaeffer, R. D., Liao, Y., Kinch, L. N., Pei, J., Shi, S., Kim, B. H., and Grishin, N. V. (2014) ECOD: an evolutionary classification of protein domains. *PLoS Comput. Biol.* **10,** e1003926 CrossRef Medline
36. Tokuriki, N., and Tawfik, D. S. (2009) Stability effects of mutations and protein evolvability. *Curr. Opin. Struct. Biol.* **19,** 596–604 CrossRef Medline
37. Gobeil, S., Rodrigue, M. A., Moisan, S., Nguyen, T. D., Polansky, J. R., Morissette, J., and Raymond, V. (2004) Intracellular sequestration of hetero-oligomers formed by wild-type and glaucoma-causing myocilin mutants. *Invest. Ophthalmol. Vis. Sci.* **45,** 3560–3567 CrossRef Medline
38. Zhou, Z., and Vollrath, D. (1999) A cellular assay distinguishes normal and mutant TIGR/myocilin protein. *Hum. Mol. Genet.* **8,** 2221–2228 CrossRef Medline

39. Stothert, A. R., Fontaine, S. N., Sabbagh, J. J., and Dickey, C. A. (2016) Targeting the ER-autophagy system in the trabecular meshwork to treat glaucoma. *Exp. Eye Res.* **144,** 38–45 CrossRef Medline
40. Huard, D. J. E., Crowley, V. M., Du, Y., Cordova, R. A., Sun, Z., Tomlin, M. O., Dickey, C. A., Koren, J., 3rd, Blair, L., Fu, H., Blagg, B. S. J., and Lieberman, R. L. (2018) Trifunctional high-throughput screen identifies promising scaffold to inhibit Grp94 and treat myocilin-associated glaucoma. *ACS Chem. Biol.* **13,** 933–941 CrossRef Medline
41. Joe, M. K., Sohn, S., Hur, W., Moon, Y., Choi, Y. R., and Kee, C. (2003) Accumulation of mutant myocilins in ER leads to ER stress and potential cytotoxicity in human trabecular meshwork cells. *Biochem. Biophys. Res. Commun.* **312,** 592–600 CrossRef Medline
42. Anholt, R. R. (2014) Olfactomedin proteins: central players in development and disease. *Front. Cell Dev. Biol.* **2,** 6 CrossRef Medline
43. Stone, E. M., Fingert, J. H., Alward, W. L., Nguyen, T. D., Polansky, J. R., Sunden, S. L., Nishimura, D., Clark, A. F., Nystuen, A., Nichols, B. E., Mackey, D. A., Ritch, R., Kalenak, J. W., Craven, E. R., and Sheffield, V. C. (1997) Identification of a gene that causes primary open angle glaucoma. *Science* **275,** 668–670 CrossRef Medline
44. Wiggs, J. L., Allingham, R. R., Vollrath, D., Jones, K. H., De La Paz, M., Kern, J., Patterson, K., Babb, V. L., Del Bono, E. A., Broomer, B. W., Pericak-Vance, M. A., and Haines, J. L. (1998) Prevalence of mutations in TIGR/myocilin in patients with adult and juvenile primary open-angle glaucoma. *Am. J. Hum. Genet.* **63,** 1549–1552 CrossRef Medline
45. Jain, A., Zode, G., Kasetti, R. B., Ran, F. A., Yan, W., Sharma, T. P., Bugge, K., Searby, C. C., Fingert, J. H., Zhang, F., Clark, A. F., and Sheffield, V. C. (2017) CRISPR-Cas9-based treatment of myocilin-associated glaucoma. *Proc. Natl. Acad. Sci. U.S.A.* **114,** 11199–11204 CrossRef Medline
46. Stothert, A. R., Suntharalingam, A., Huard, D. J., Fontaine, S. N., Crowley, V. M., Mishra, S., Blagg, B. S., Lieberman, R. L., and Dickey, C. A. (2014) Exploiting the interaction between Grp94 and aggregated myocilin to treat glaucoma. *Hum. Mol. Genet.* **23,** 6470–6480 CrossRef Medline
47. Stothert, A. R., Suntharalingam, A., Tang, X., Crowley, V. M., Mishra, S. J., Webster, J. M., Nordhues, B. A., Huard, D. J. E., Passaglia, C. L., Lieberman, R. L., Blagg, B. S. J., Blair, L. J., Koren, J., 3rd, and Dickey, C. A. (2017) Isoform-selective Hsp90 inhibition rescues model of hereditary open-angle glaucoma. *Sci. Rep.* **7,** 17951 CrossRef Medline
48. Schultz, J. E., and Natarajan, J. (2013) Regulated unfolding: a basic principle of intraprotein signaling in modular proteins. *Trends Biochem. Sci.* **38,** 538–545 CrossRef Medline
49. Mancl, J. M., Ray, W. K., Helm, R. F., and Schubot, F. D. (2019) Helix cracking regulates the critical interaction between RetS and GacS in pseudomonas aeruginosa. *Structure* **27,** 785–793.e5 CrossRef Medline
50. Whitford, P. C., Miyashita, O., Levy, Y., and Onuchic, J. N. (2007) Conformational transitions of adenylate kinase: switching by cracking. *J. Mol. Biol.* **366,** 1661–1671 CrossRef Medline
51. Hartmann, M. D. (2017) Functional and structural roles of coiled coils. *Subcell. Biochem.* **82,** 63–93 CrossRef Medline
52. Colón, W., Church, J., Sen, J., Thibeault, J., Trasatti, H., and Xia, K. (2017) Biological roles of protein kinetic stability. *Biochemistry* **56,** 6179–6186 CrossRef Medline
53. Tokuriki, N., Stricher, F., Serrano, L., and Tawfik, D. S. (2008) How protein stability and new functions trade off. *PLoS Comput. Biol.* **4,** e1000002 CrossRef Medline
54. Tokuriki, N., and Tawfik, D. S. (2009) Protein dynamism and evolvability. *Science* **324,** 203–207 CrossRef Medline
55. Stumpff, F., and Wiederholt, M. (2000) Regulation of trabecular meshwork contractility. *Ophthalmologica* **214,** 33–53 CrossRef Medline
56. Jakobi, A. J., Mashaghi, A., Tans, S. J., and Huizinga, E. G. (2011) Calcium modulates force sensing by the von Willebrand factor A2 domain. *Nat. Commun.* **2,** 385 CrossRef Medline
57. Wang, N., Tytell, J. D., and Ingber, D. E. (2009) Mechanotransduction at a distance: mechanically coupling the extracellular matrix with the nucleus. *Nat. Rev. Mol. Cell Biol.* **10,** 75–82 CrossRef Medline
58. Mayer, S., Rüdiger, S., Ang, H. C., Joerger, A. C., and Fersht, A. R. (2007) Correlation of levels of folded recombinant p53 in *Escherichia coli* with thermodynamic stability *in vitro*. *J. Mol. Biol.* **372,** 268–276 CrossRef Medline
59. Reich, L., Becker, M., Seckler, R., and Weikl, T. R. (2009) *In vivo* folding efficiencies for mutants of the p22 tailspike β-helix protein correlate with predicted stability changes. *Biophys. Chem.* **141,** 186–192 CrossRef Medline
60. Gershenson, A., Gierasch, L. M., Pastore, A., and Radford, S. E. (2014) Energy landscapes of functional proteins are inherently risky. *Nat. Chem. Biol.* **10,** 884–891 CrossRef Medline
61. Humphrey, W., Dalke, A., and Schulten, K. (1996) VMD: visual molecular dynamics. *J. Mol. Graph.* **14,** 33–38, 27–28 CrossRef Medline
62. Jorgensen, W. L., Chandrasekhar, J., Madura, J. D., Impey, R. W., and Klein, M. L. (1983) Comparison of simple potential functions for simulating liquid water. *J. Chem. Phys.* **79,** 926–935 CrossRef
63. Phillips, J. C., Braun, R., Wang, W., Gumbart, J., Tajkhorshid, E., Villa, E., Chipot, C., Skeel, R. D., Kalé, L., and Schulten, K. (2005) Scalable molecular dynamics with NAMD. *J. Comput. Chem.* **26,** 1781–1802 CrossRef Medline
64. Case, D. A., Betz, R. M., Botello-Smith, W., Cerutti, D. S., Cheatham, T. E. I., Darden, T. A., Duke, R. E., Giese, T. J., Gohlke, H., Goetz, A. W., Homeyer, N., Izadi, S., Janowski, P., Kaus, J., Kovalenko, A., *et al.* (2016) *AMBER 16*, University of California, San Francisco
65. Best, R. B., Zhu, X., Shim, J., Lopes, P. E., Mittal, J., Feig, M., and Mackerell, A. D., Jr. (2012) Optimization of the additive CHARMM all-atom protein force field targeting improved sampling of the backbone ϕ, ψ and side-chain χ_1 and χ_2 dihedral angles. *J. Chem. Theory Comput.* **8,** 3257–3273 CrossRef Medline
66. Feller, S. E., Zhang, Y. H., Pastor, R. W., and Brooks, B. R. (1995) Constant-pressure molecular-dynamics simulation—the Langevin piston method. *J. Chem. Phys.* **103,** 4613–4621 CrossRef
67. Darden, T., York, D., and Pedersen, L. (1993) Particle mesh Ewald—an $N\cdot\log(N)$ method for Ewald sums in large systems. *J. Chem. Phys.* **98,** 10089–10092 CrossRef
68. Otwinowski, Z., and Minor, W. (1997) Processing of x-ray diffraction data collected in oscillation mode. *Methods Enzymol.* **276,** 307–326 CrossRef Medline
69. McCoy, A. J., Grosse-Kunstleve, R. W., Adams, P. D., Winn, M. D., Storoni, L. C., and Read, R. J. (2007) Phaser crystallographic software. *J. Appl. Crystallogr.* **40,** 658–674 CrossRef Medline
70. Adams, P. D., Afonine, P. V., Bunkóczi, G., Chen, V. B., Davis, I. W., Echols, N., Headd, J. J., Hung, L. W., Kapral, G. J., Grosse-Kunstleve, R. W., McCoy, A. J., Moriarty, N. W., Oeffner, R., Read, R. J., Richardson, D. C., *et al.* (2010) Phenix: a comprehensive python-based system for macromolecular structure solution. *Acta Crystallogr. D Biol. Crystallogr.* **66,** 213–221 CrossRef Medline
71. Emsley, P., Lohkamp, B., Scott, W. G., and Cowtan, K. (2010) Features and development of Coot. *Acta Crystallogr. D Biol. Crystallogr.* **66,** 486–501 CrossRef Medline
72. Afonine, P. V., Grosse-Kunstleve, R. W., Echols, N., Headd, J. J., Moriarty, N. W., Mustyakimov, M., Terwilliger, T. C., Urzhumtsev, A., Zwart, P. H., and Adams, P. D. (2012) Towards automated crystallographic structure refinement with phenix.refine. *Acta Crystallogr. D Biol. Crystallogr.* **68,** 352–367 CrossRef Medline

Stable calcium-free myocilin olfactomedin domain variants reveal challenges in differentiating between benign and glaucoma-causing mutations

Shannon E. Hill, Michelle S. Kwon, Mackenzie D. Martin, Amirthaa Suntharalingam, Anthony Hazel, Chad A. Dickey, James C. Gumbart and Raquel L. Lieberman

J. Biol. Chem. 2019, 294:12717-12728.
doi: 10.1074/jbc.RA119.009419 originally published online July 2, 2019